Supplementary information

Optimizing interface concentration and electric fields for enhanced lithium deposition behavior in lithium metal anodes

Jiaxiang Liu,[a] Haiming Hua,[b] Jie Lin,[e] Yongliang Deng,[b] Nanbiao Pei,[b] Peng Zhang, *[ac] Jin-Chao Dong,*[a] Jian-Feng Li*[abc] Jinbao Zhao*[abcd]

[a]College of Energy, Xiamen University, Xiamen 361102, P.R. China.

[b]College of Chemistry and Chemical Engineering, Xiamen University, Xiamen 361005, P. R. China.

[c]Tan Kah Kee Innovation Laboratory (lKKEM), Xiamen 361005, China.

[d]State-Province Joint EngineeringLaboratory of PowerSource Technology for New Energy Vehicle, State Key Laboratory of Physical Chemistry of Solid Surfaces, Engineering Research Center of Electrochemica Technology, Ministry of Education, Collaborative Innovation Center of Chemistry for Energy Materials, Xiamen University, Xiamen, 361005，PR China.

[e]School of Mechanical and Aerospace Engineering, Queen's University Belfast Ashby Building, Stranmillis Road, Belfast BT9 5AH, United Kingdom

E-mail:pengzhang@xmu.edu.cn; jcdong@xmu.edu.cn; Li@xmu.edu.cn; jbzhao@xmu.edu.cn

Experimental Details

Fabrication of simulated coin cell for in-situ Raman measurement

The in-situ Raman measurement is conducted in a simulated coin cell to approach the actual operating condition in laboratory. The current collector is Cu foil washed by acetone, 3 M HCl, deionized water and ethyl alcohol for three times respectively to wipe off the surface impurity and oxidation layer. The positive shell (CR2016) and Li foil is cut out a hole of 4 mm in diameter. The separator (Celgard 2500) is cut out a hole of 3 mm in diameter. The simulated coin cell is fabricated by negative shell, Cu current collector, holed separator, holed Li foil and holed positive shell from bottom to top. 30 μL electrolyte is added in each cell. Then, the simulated coin cell is sealed in a homemade Raman device, with a quartz window of 6 mm in diameter for observation. The Raman laser can hit at the surface of Cu foil through the holed Li foil and separator. The Cu foil can enhance Raman scattering to some extent. All simulated coin cells were assembled in glove box (Ar, O_2 < 0.5 ppm, H_2O < 0.5 ppm)

In situ Raman experimental setup

The electrochemical in-situ Raman measurements were conducted on a confocal microscope Raman system, including EC-Raman (Xiamen SHINs Technology) and XploRA (HORIBA). A He-Ne laser with an excitation wavelength of 532 nm and a 50× microscope objective with a numerical aperture of 0.55 were used in all measurements. Raman frequency was calibrated by a Si wafer before each experiment. The galvanostatic polarization of the simulated coin cell is controlled by the battery test system (Newwell, CT2001A). The galvanostatic current of 0.1 mA cm^{-2} is applied on each cell to drive the deposition of lithium.

Materials preparation

Preparation of electrolytes:

EC/DEC-1M-$LiPF_6$: Ethylene carbonate/Diethyl carbonate (1:1, v/v) with 1M lithium hexafluorophosphate;

EC/DEC-1M-LiTFSI: Ethylene carbonate/Diethyl carbonate (1:1, v/v) with 1 M lithium bis(trifluoromethylsulfonyl)imide;

DOL/DME-1M-LiTFSI: 1,3-dioxolane/1,2-dimethoxyethane (1:1, v/v) with 1M lithium bis(trifluoromethylsulfonyl)imide.

Preparation of LiTVI: The lithium ((trifluoromethanesulfonyl)(vinylsulfonyl)imide) (LiTVI) is synthesized by the reaction between 2-chloroethanesulfonyl chloride and trifluoromethanesulfonamide, followed by ion-exchange reaction[1] First, 18.0 g Trifluoromethanesulfonamide and 36.65 g triethylamine was dissolved in 150 mL acetonitrile in a 500 mL round-bottom flask. Then, 20.67 g 2-chloroethanesulfonyl chloride dissolved in 80 mL acetonitrile was added to the solution for 1 h through the dropping funnel at 0 °C. The mixture was stirred for 21 h at 25 °C. The precipitated salt was filtered off and the solution was concentrated under reduced pressure. The crude product was then dissolved in 200 mL acetonitrile. Further, 33.5 g Potassium carbonate was added to the solution, and the mixture was stirred for 4 h at 0 °C. The solution was filtered and dried under vacuum at ambient temperature. The intermediate product, potassium (trifluoromethanesulfonyl)(vinylsulfonyl)imide (KTVI), was further purified by washing with ether and recrystallization with acetone. For ion-exchange reaction, 20.0 g KTVI was dissolved in 50 mL acetonitrile and 11.6 g lithium perchlorate trihydrate was added. The mixture was stirred for 12 h at 25 °C. The insoluble part was filtered off, and the product was obtained by lyophilization for 1 week. The final product LiTVI was recrystallized in acetonitrile, dried under high vacuum at 50 °C for 48 h, and stored in an Ar-filled glovebox before use.

Preparation of LiTVI-PEO and HACI@Li electrode: 2.39 g polyethylene oxide (PEO, M_w=60, 000) and 1.33g LiTVI was dissolved in 80 mL acetonitrile (O/Li=10:1). Then, the solution was bubbled with argon for 30 min to remove the dissolved oxygen and sealed in polypropylene bottle. Further, the solution was exposed under the ^{60}Co Gamma ray at room temperature with a total dose of 50 kGy. The obtained product was extracted and washed by cold diethyl ether for three times and heated at 80 ℃ to volatilize residual solvent. The final product LiTVI-PEO was collected for use. Then, 100 mg LiTVI-PEO was dissolved in 10 mL tetrahydrofuran (THF) and obtained the

treating solution. 40 μL treating solution was drip casted on the surface of polished Li foil (Φ=12 mm) and dried under high vacuum for 1 h to prepare the HACI@Li electrode. All procedures were conducted in glove box (Ar, O_2 < 0.5 ppm, H_2O < 0.5 ppm).

Preparation of the high-loading cathode: NCM523, acetylene black (AB) and poly (vinylidene fluoride) (PVDF) were mixed at mass ratios of 94:3:3, respectively. Nmethyl-2-pyrrolidone (NMP) solvent was added to the mixture to adjust to the proper viscosity. After that, the slurry was stirred for 30 min, then coated on Al foil and dried under vacuum at 80 ℃ for 12 h. The cathodes were punched into pieces with a diameter of 12 mm. The mass loading of the active cathode material is about 14 mg cm^{-2}.

Characterization and electrochemical measurement

Ex situ Raman measurements were conducted using a He-Ne laser with an excitation wavelength of 532 nm and a 50× microscope objective with a numerical aperture of 0.55.

The ionic conductivity of electrolyte was measured by electrochemical workstation (CH Instruments Ins, CHI660D) and a conductivity electrode (Leici, DJS-1C).

The cationic transference number of electrolyte is measured by alternating current (AC) impedance and steady-state current method (Metrohm Autolab PGSTAT-302N) in Li||Li symmetrical cell[2]. The calculation formula is shown as follows:

$$t_+ = \frac{I_s(\Delta V - I_0 R_0)}{I_0(\Delta V - I_s R_s)} \quad (1)$$

where I_0 and I_s are the initial and steady-state current density respectively; R_0 and R_s are the interfacial impedance before and after the polarization by the AC impedance method respectively; ΔV is the applied polarization voltage (10 mV).

The activation energy is closely correlated with the charge transfer resistance which can be measured via EIS at different temperatures. The *E*a can be quantitatively described using the Arrhenius equation[3]:

$$\frac{1}{R_{SEI}} = Aexp(-\frac{E_a}{RT}) \quad (2)$$

where R_{SEI} is the charge transfer resistance, A is the frequency factor, R is the ideal gas constant and T is the absolute temperature. All R_{SEI} values were fitted based on the EIS curves of pure Li and HACI@Li symmetrical cells at various temperatures ranging from 25 °C to 60 °C.

The molecule structure of LiTVI salt and LiTVI-PEO is measured by A Fourier transform infrared spectrometer (FT-IR, Thermo Fisher Scientific Inc., Nicolet IS5 spectrometer,). ^{1}H NMR and ^{19}F spectra of LiTVI salt and LiTVI-PEO were acquired by the AVANCE NEO 500 MHz Digital FT NMR Spectrometer, and a capillary tube filled with 0.1 M $LiClO_4$ in D_2O was used to lock the field.

The morphology and element distribution were obtained by Scanning electron microscopy (HITACHI, TM3030) and energy dispersive X-Ray spectroscopy (Oxford, AZTECONE). The analysis of the composition on electrode was conducted by X-ray photoelectron spectroscopy (Thermo Fisher, Escalab Xi+). The electrochemical impedance was measured from 0.1 Hz to 100 kHz by Electrochemical impedance spectroscopy (Solartron, Modulab 1260). The Nyquist plots with one semicircle can be interpreted using series-wound equivalent analogs of retractor-capacitor (RC) circuits in series, while the semicircle diameter is proportional to the interfacial impedance of the SEI film. The in-situ observation images of lithium deposition were obtained by in situ microscopic imaging batteries. The electrochemical performance of Li||Li symmetrical cells were tested in 2032-type coin cells. The full cells were assembled in 2016-type coin cells by high-loading cathode and limited lithium film (50 μm in thickness). 1 M $LiPF_6$ dissolved in Ethylene carbonate/Diethyl carbonate (EC/DEC, 1:1, v/v), with 5 wt% fluoroethylene carbonate (FEC) as additive, was used as electrolyte for testing electrochemical performance of symmetrical cells and full cells. 75 μL electrolyte was added to each coin cell. All coin cells were assembled in glove box (Ar, O_2 < 0.5 ppm, H_2O < 0.5 ppm) with Celgard 2500 separators. The cycling performance of all cells were tested by Battery Tester (Land, CT2001A).

Molecular dynamics simulation details

Molecular dynamics (MD) simulation was performed by Gromacs2018.8[4] software to study the electrolyte and metal/electrolyte interface structure at different potentials and concentrations. The model of PEO based polymer single ion conductor contains 100 EO structural units. 10 TVI groups are evenly grafted on main chain. All molecules used in MD simulation were shown as below:

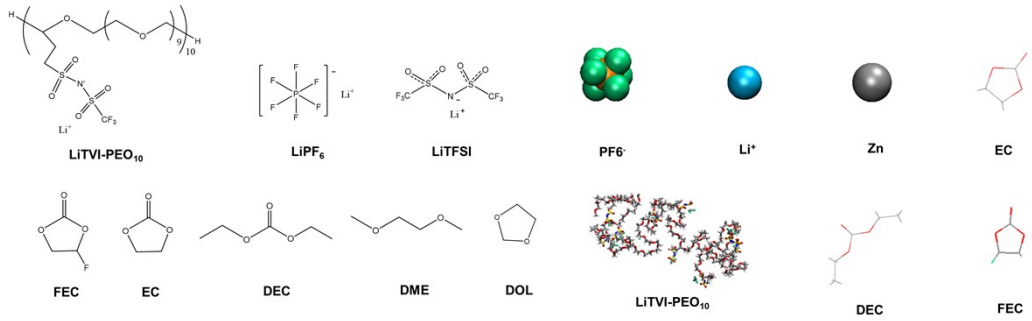

The OPLS-AA[5] force field parameters of lithium salts, solvents and polymers were generated with Sobtop[6] program. Leonard-Jones parameters of metal zinc atoms were set as σ = 2.44 Å, ε = 3.022 kJ/mol, which showed good accuracy in the interface in our previous works[7, 8]. It is worth noting that classical molecular dynamics is only able to describe metal atoms by two parameters σ (van der Waals potential trap distance) and ε (van der Waals potential trap depth), thus the metal slab does not contain the chemical properties. Thus, the zinc metal slab was only a general representative of the metal plate, because the zinc slab is not easy to deform in the heating and annealing simulation. RESP[9] atom charges calculated by Gaussian09 E01[10] and Multiwfn[11] software were used to describe electrostatic interactions. Atomic charges of all ions were multiplied by scale factor 0.78 to correct the polarization effect of ions. A constraint Potential (force constant = 1×10^5 kJ/mol) in the X, Y and Z axes for Zn atoms in electrode was used to maintain the structure of metallic zinc. The electrode potential was controlled by the charge density of the Zinc metal surface. The interface capacitance was set to 40 μF/cm^2.

The composition of the interface model was shown in Table S4. An 8-layer slab contained 3680 Zn atoms was used as the model of inert metal electrode. The boxes of

polymer-free system were built by filling molecules randomly. For polymer covered surface, 12 polymer models and 120 Li ions were spread on the electrode surface. After 40 ns NPT pre-equilibration at 498.2 K and 100 bar, liquid electrolytes were filled into the boxes. All the boxes were first submitted to energy minimization using the steepest descent method. The equilibrium simulation was carried out with NPT ensemble at 298.2 K and 1bar for 20 ns; The production simulation was carried out with NVT ensemble at 298.2 K for 20 ns.

To simulate the ion conductivity and transport number, an NVT simulation with an electric field of 0.05 V/nm for 40 ns was performed, the conductivity was calculated by formula as follows. v is average drift rate; c is ion concentration; E is Electric field strength; Z is Ion charge; F is Faraday constant.

$$\sigma = \frac{|v^+|}{E} \cdot c^+ \cdot |Z^+| \cdot F + \frac{|v^-|}{E} \cdot c^- \cdot |Z^-| \cdot F \quad (3)$$

$$t = \frac{\sigma^+}{\sigma^+ + \sigma^-} \quad (4)$$

The distribution of number density was calculated by Gromacs2018.8. VMD[12] software was used to visualize the systems and get the ion association state.

Finite element analysis details

Electrolyte modeling

Bulk electrolyte:

In bulk electrolyte, the movement of the ions can be driven by migration in response to an electric field, diffusion due to concentration gradient, and convection from bulk fluid motion. The net flux of an ionic species is the sum of these effects and is described by Nernst-Planck equation[13] as follows:

$$\mathbf{N}_i = -D_i \nabla c_i - z_i u_i F c_i \nabla \phi + c_i \mathbf{v} \quad (5)$$

where subscript $i \in \{+,-\}$ denotes the ionic species of cation or anion, $\mathbf{N}_i$ denotes the

flux density of species i, c_i is the species concentration in the electrolyte, D_i is the diffusivity of species i in the electrolyte, z_i is the charge number of the ionic species, u_i is the mobility of the charged species, F is Faraday's constant, ϕ is the electric potential in the electrolyte, and **v** is the velocity of the bulk electrolyte.

In Eqn. (4), the first term on the right side of the equation is diffusion flux from Fick's law, the second term is the migration flux, and the last term represents convection. The convection effect is normally neglected in static cells (**v**=**0**). When there are no homogeneous reactions in the electrolyte, the species should satisfy a mass balance equation as below:

$$\frac{\partial c_i}{\partial t} + \nabla \cdot \mathbf{N}_i = 0 \tag{6}$$

In addition, the bulk electrolyte should hold the electroneutrality condition given by the following expression:

$$\sum_i z_i c_i = 0 \tag{7}$$

The current (**i**) in the electrolyte is the net flux of all charged species, expressed as:

$$\mathbf{i} = \sum_i z_i F \mathbf{N}_i \tag{8}$$

Electrical double layer:

When an electrode is in contact with an electrolyte, an electric field will be established at their interface. This leads to a charge separation at the interface, where an excess of charges occurs on the electrode surface, and to counterbalance these charges, opposite charges in the electrolyte will accumulate at the interface. The two layers of opposite charges are typically separated by a single layer of solvent molecules that adhere to the electrode surface, forming an electrical double layer (EDL) in the very vicinity of an electrode surface (within a few nanometers), which is approximate to a conventional capacitor. Hence, the EDL will exhibit a capacitive behavior known as the double-layer capacitance.

However, the real EDL can be much more complex than ideally polarized charges at the electrode-electrolyte interface, which was first described by Helmholtz[14] The most

common representation of EDL is the Gouy–Chapman–Stern (GCS) model[15-17] where the EDL consists of an inner compact layer and an outer diffuse layer. The compact layer is in contact with the electrode surface with charged ions absorbed by the surface through strong electrostatic interactions. In the diffuse layer, ions will move due to Brownian motion, while being attracted and repelled by unscreened excess charge on the electrode.

In EDL, the electroneutrality assumption is no longer valid due to the polarization of charged species, and more physics need to be considered for accurate predictions of ion and potential distributions.

In addition to the Nernst-Planck equation which models mass transport of ions, the Poisson equation is introduced to describe the charge density and electric field, expressed as below:

$$\nabla \cdot (-\varepsilon \nabla \phi) = \rho \tag{9}$$

where $\varepsilon = \varepsilon_r \varepsilon_0$ is the permittivity of the electrolyte. ε_r is the relative permittivity (dielectric constant), ε_0=8.8542×10^{-12} F/m is the vacuum permittivity, and ρ is the charge density which satisfies:

$$\rho = \sum_i z_i c_i \tag{10}$$

Inside the compact double layer, there is no charge (ρ=0), and the electric field is constant with uniform permittivity. Hence, the electric potential in the compact layer can be expressed as:

$$\mathbf{n} \cdot (-\varepsilon \nabla \phi) = -\frac{\varepsilon \phi_\Delta}{\lambda_s} \tag{11}$$

where $\phi_\Delta = \phi_s - \phi$. ϕ_s is the potential on the electrode surface and λ_s is the thickness of compact layer.

In Poisson-Boltzmann theory[18, 19], the diffuse layer is thought to be in direct contact with the charged electrode surface whose electric potential is known, and the potential difference between the electrode and the diffuse layer (across the compact layer) is experimentally measurable. The thickness of the diffuse layer is assumed to be the

Debye length (λ_D)[20], defined as follows for a binary electrolyte:

$$\lambda_D = \sqrt{\frac{\varepsilon RT}{2z_i^2 F^2 c_0}} \tag{12}$$

where c_0 is the concentration of bulk electrolyte, and T is absolute temperature.

The electrochemical reactions are assumed to take place outside the compact layer and at the boundary between the compact and diffuse layers. The reaction current density (i) for lithium plating/stripping can be calculated from Butler-Volmer kinetics:

$$i = i_0 \left[\exp\left(\frac{\alpha_a F \eta}{RT} \right) - \exp\left(-\frac{\alpha_c F \eta}{RT} \right) \right] \tag{13}$$

where $\eta = \phi_s - \phi - E_{eq}$ is the surface overpotential, and E_{eq} is the equilibrium potential of the solid electrode vs. Li/Li^+. i_0 is the exchange current density, and α_a and α_c are the anodic and cathodic charge transfer coefficient, respectively.

Besides, to enable the electrochemical reactions in a symmetric Li-Li cell, an external current is applied to the cathode, which yields a Neumann-type boundary condition on the cathode surface:

$$-\mathbf{n} \cdot \mathbf{i} = i_{app} \tag{14}$$

where i_{app} is the applied current density.

Numerical simulation

The above model for the bulk electrolyte and the electrical double layer at the electrode-electrolyte interface is established in the COMSOL Multiphysics environment. The partial differential equations are numerically solved using the finite element method. Key parameters of different electrolytes used in the model simulations are listed in Table S5. All parameters are obtained from experiments and references[21, 22].

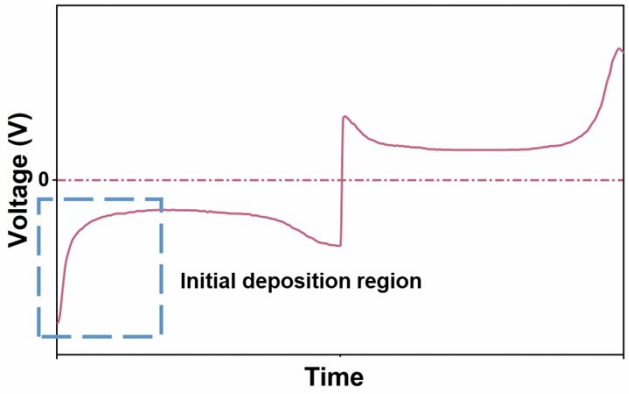

Fig. S1: Schematic plot of the typical voltage profiles of galvanostatic plating and stripping of lithium.

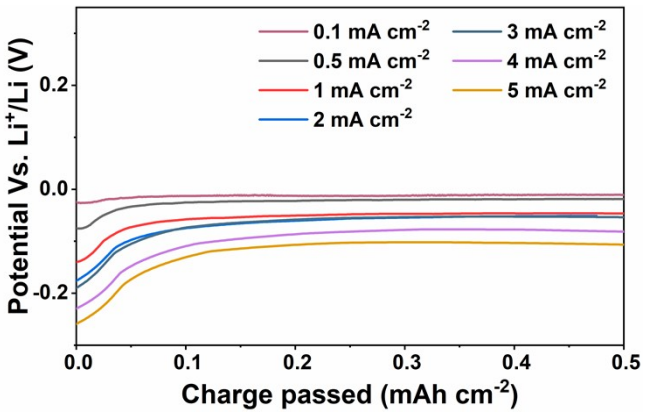

Fig. S2: Potential profiles of galvanostatic lithium deposition at different current density in EC/DEC-1M-$LiPF_6$ electrolyte.

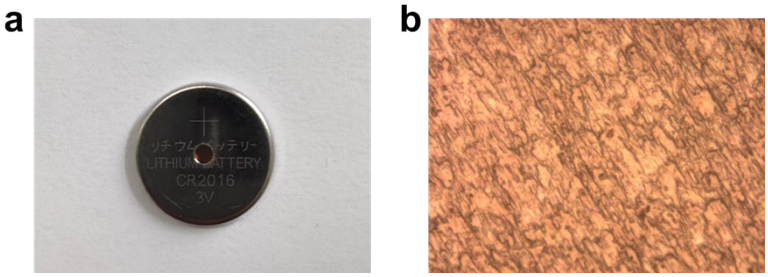

Fig. S3: Optical images of simulated coin cells: **a,** Simulated coin cell with a hole on the positive shell for Raman laser. **b,** Surface morphology of the Cu current collector for the collection of Raman signals.

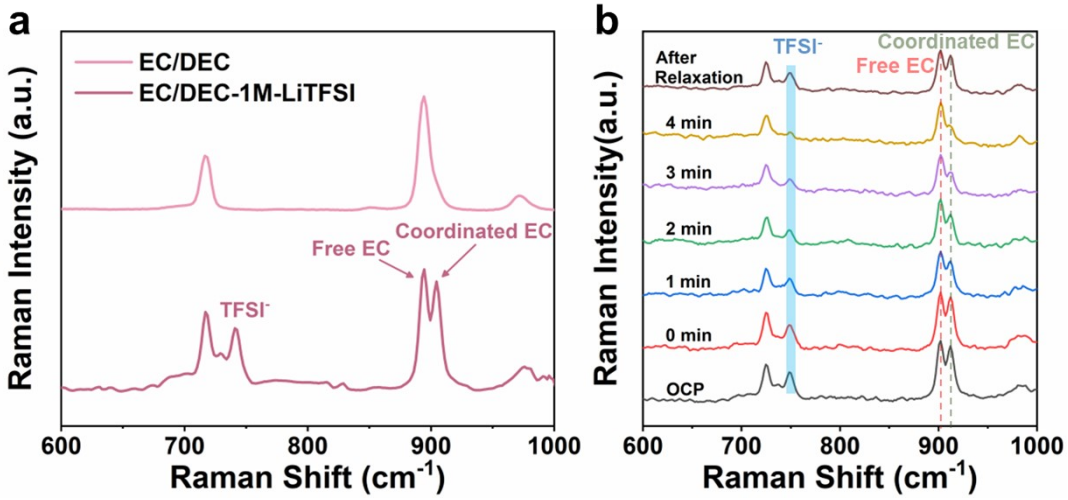

Fig. S4: Raman spectra of EC/DEC-1M-LiTFSI: **a,** Ex-situ Raman spectra of EC/DEC-1M-LiTFSI and pure solvents. **b,** Interfacial in-situ Raman spectra of EC/DEC-1M-LiTFSI at current density of 0.1 mA cm^{-2}. The peak centered at around 740 cm^{-1} can be assigned to $TFSI^{-}$[23].

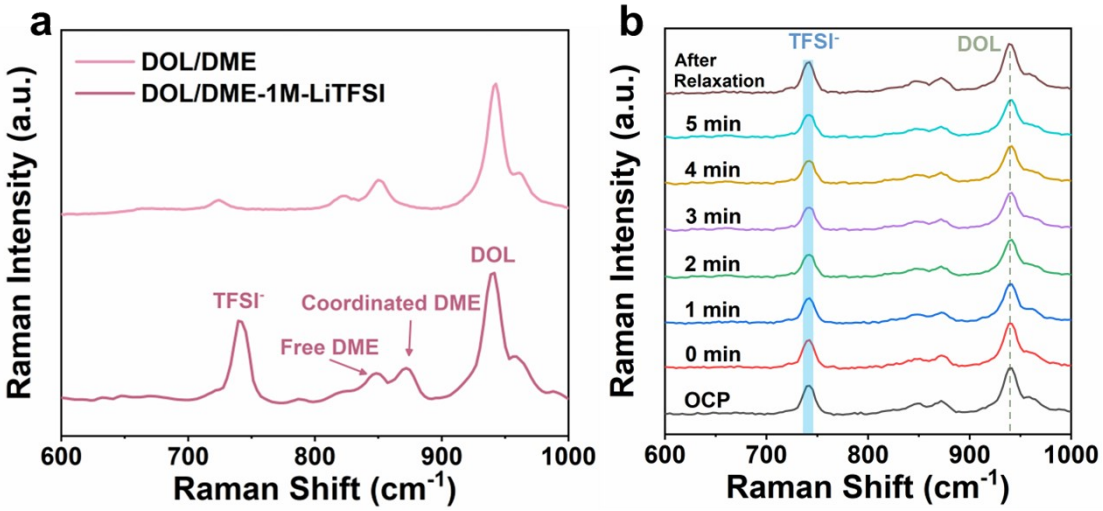

Fig. S5: Raman spectra of DOL/DME-1M-LiTFSI: **a,** Ex-situ Raman spectra of DOL/DME-1M-LiTFSI and pure solvents. **b,** Interfacial in-situ Raman spectra of DOL/DME-1M-LiTFSI at current density of 0.1 mA cm^{-2}. The peak centered at around 850 cm^{-1} and 870 cm^{-1} can be assigned to free DME and solvated DME respectively[24] and the peak centered at around 950 cm^{-1} can be assigned to DOL[25].

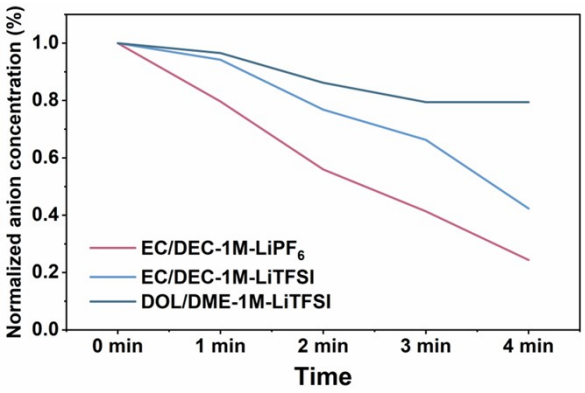

Fig. S6: Variation of the concentration of anions among the interface in different electrolyte at a current density of 0.1 mA cm^{-2}.

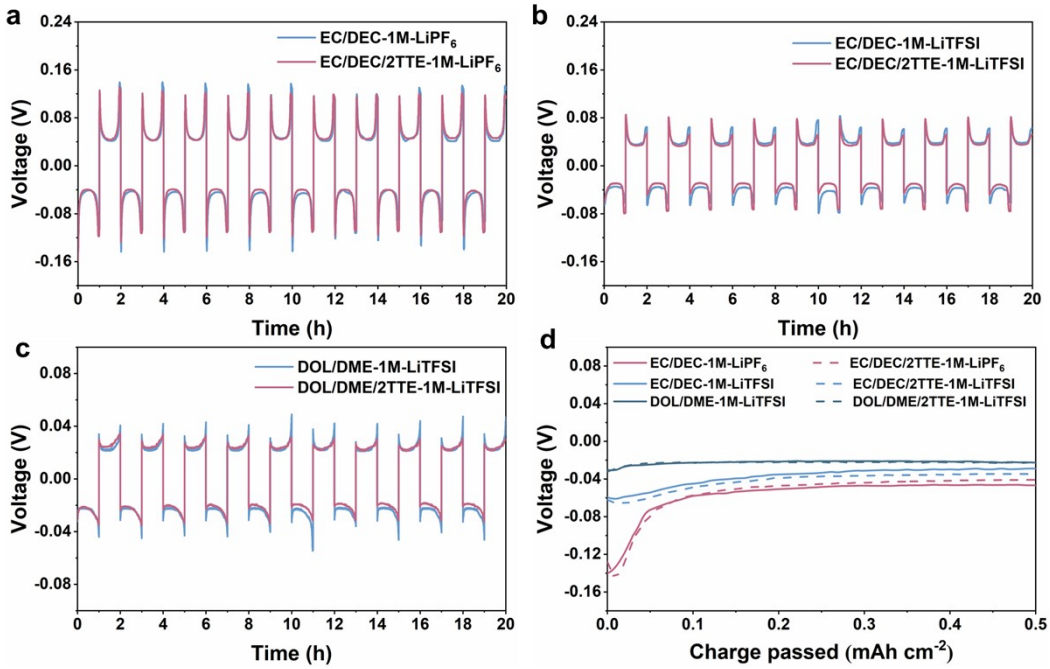

Fig. S7: Electrochemical performance of electrolytes with/without TTE: **a, b, c,** Voltage profiles of galvanostatic plating and stripping of lithium in different electrolytes with/without internal standard substance TTE. **d,** Initial voltage profiles of galvanostatic lithium deposition on lithium substrate in different electrolytes with/without internal standard substance TTE.

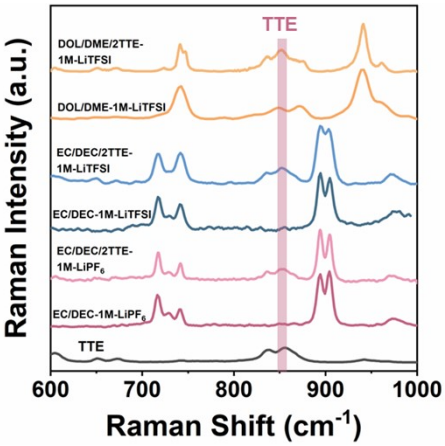

Fig. S8: Raman spectra comparison of different electrolyte with/without internal standard substance TTE.

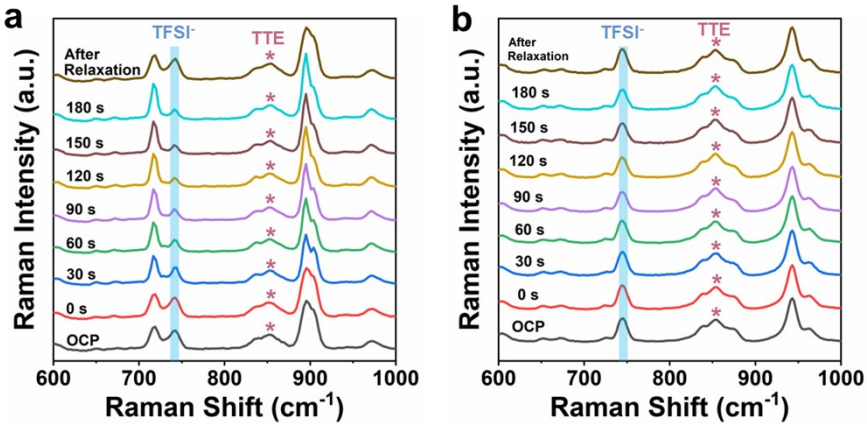

Fig. S9: Quantitative in situ Raman spectra: Interfacial in-situ Raman spectra of EC/DEC/2TTE-1M-LiTFSI (**a**) and DOL/DME/2TTE-1M-LiTFSI (**b**) at a current density of 0.1 mA cm^{-2}.

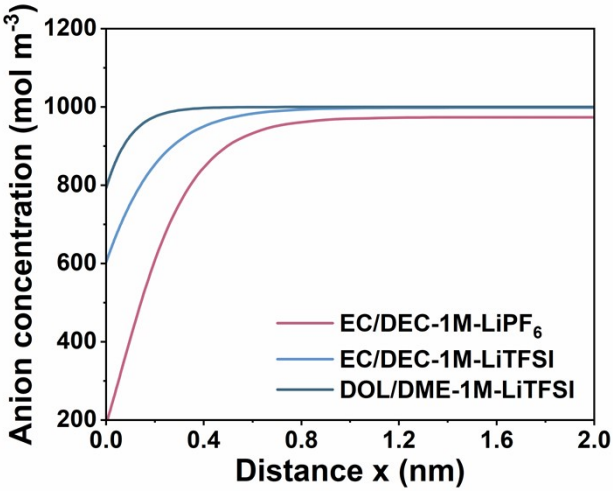

Fig. S10: Anion concentration distribution at electrolyte/electrode interface in different electrolytes obtained by FEA simulation.

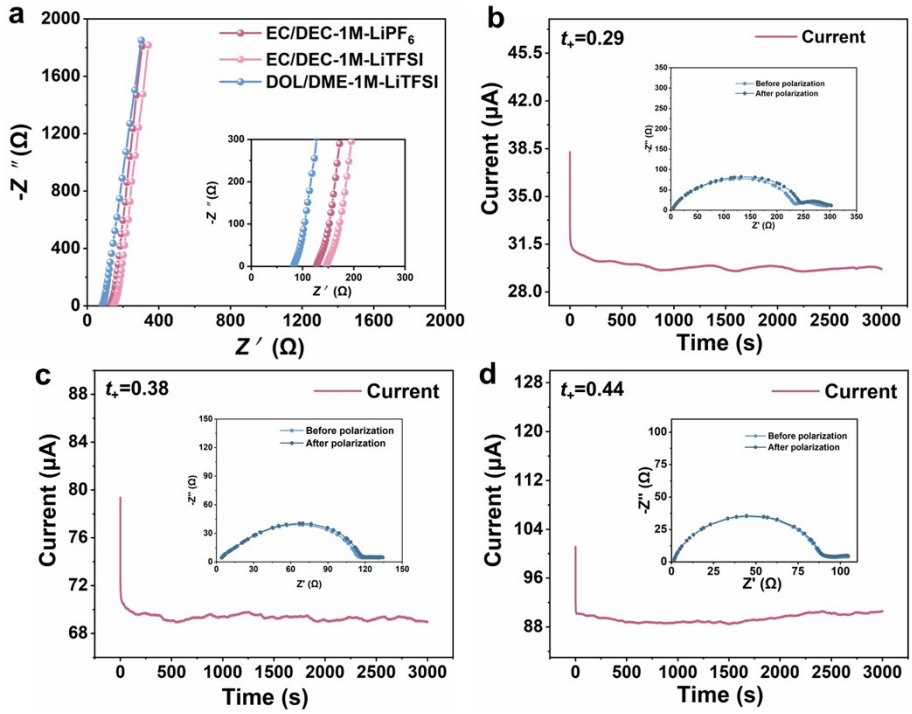

Fig. S11: Ionic conductivity and cationic transference number: **a,** Ionic conductivity of different electrolytes. Cationic transference number of EC/DEC-1M-$LiPF_6$ (**b**), EC/DEC-1M-LiTFSI (**c**) and DOL/DME-1M-LiTFSI (**d**).

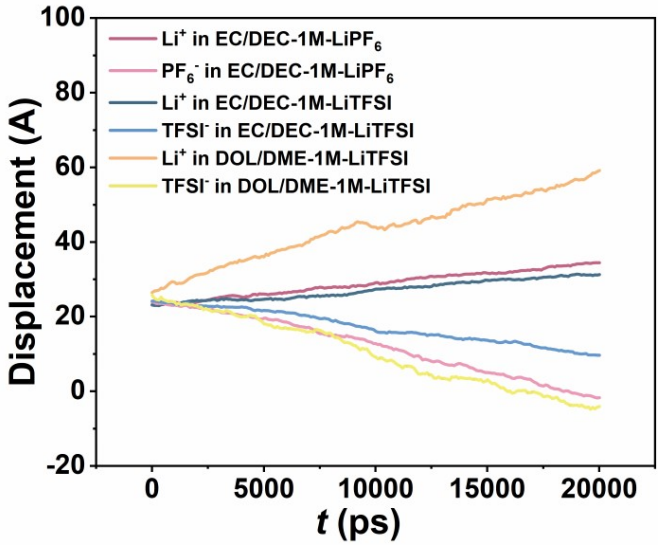

Fig. S12: MD simulation of the drift speed of Li^+ and anions in different electrolytes.

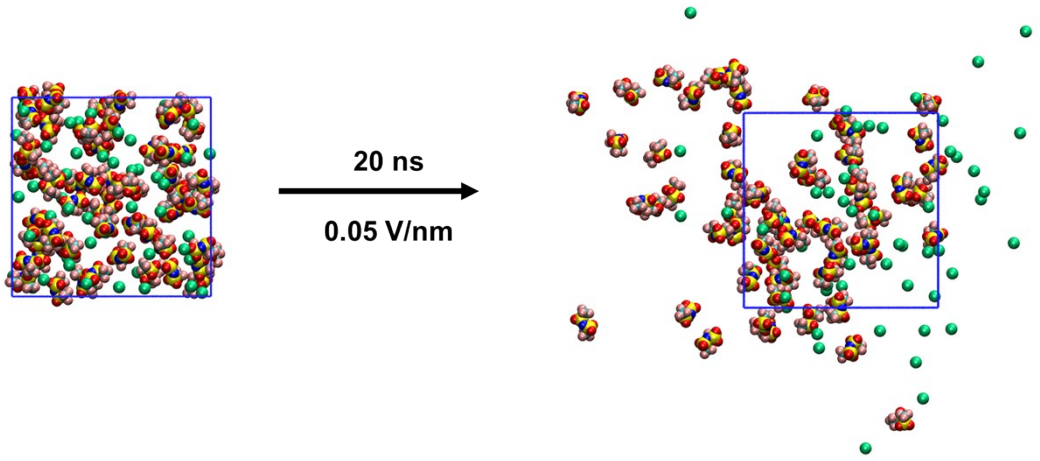

Fig. S13: MD simulation of the drift of Li^+ and anions in EC/DEC-1M-$LiPF_6$.

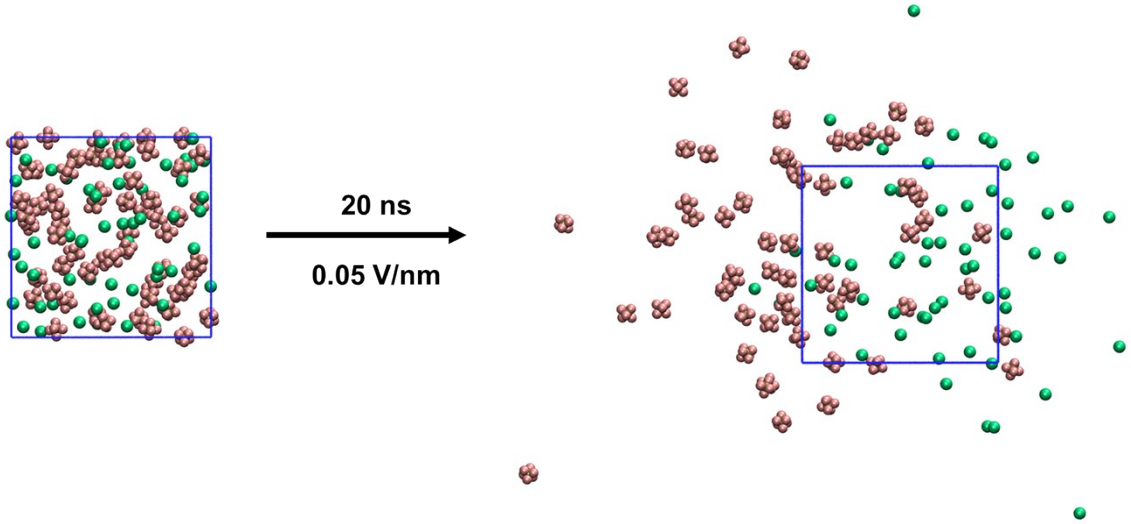

Fig. S14: MD simulation of the drift of Li^+ and anions in EC/DEC-1M-LiTFSI.

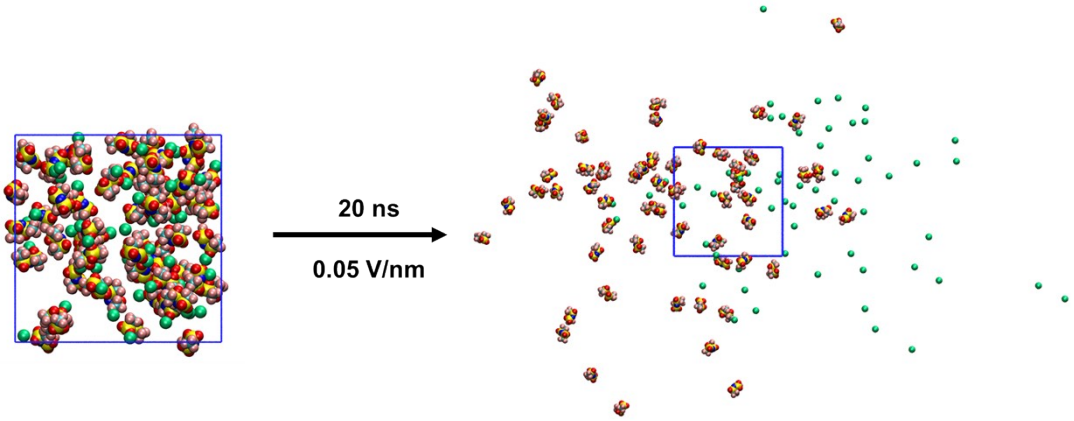

Fig. S15: MD simulation of the drift of Li^+ and anions in DOL/DME-1M-LiTFSI.

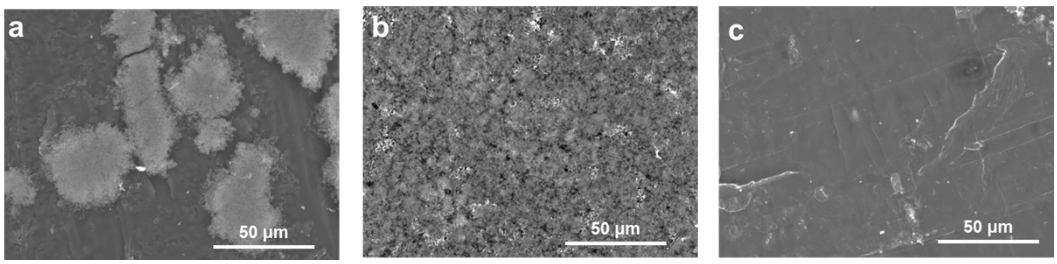

Fig. S16: Deposition morphology of lithium: Morphology of lithium deposition at current density of 5 mA cm^{-2} and capacity of 1 mAh cm^{-2} in EC/DEC-1M-$LiPF_6$ (**a**), EC/DEC-1M-LiTFSI (**b**) and DOL/DME-1M-LiTFSI (**c**).

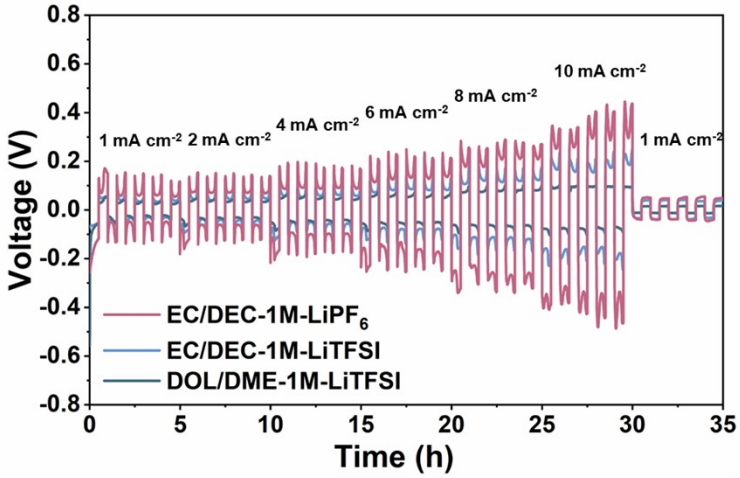

Fig. S17: Rate cycling performance of Li||Li symmetric cells with different electrolytes.

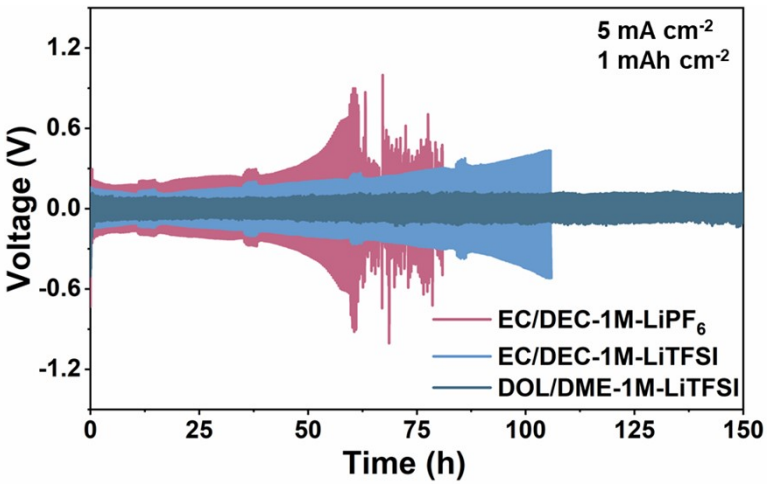

Fig. S18: Cycling performance of Li||Li symmetric cells with different electrolytes at current density of 5 mA cm^{-2} and capacity of 1 mAh cm^{-2}.

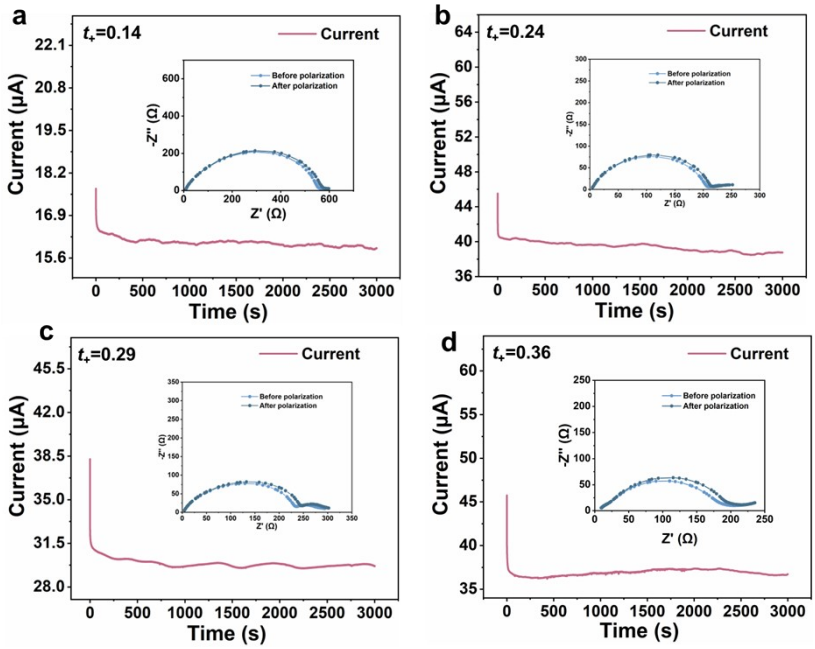

Fig. S19: Cationic transference number: Cationic transference number of EC/DEC-0.1M-$LiPF_6$ (**a**), EC/DEC-0.5M-$LiPF_6$ (**b**), EC/DEC-1M-$LiPF_6$ (**c**) and EC/DEC-3M-$LiPF_6$ (**d**).

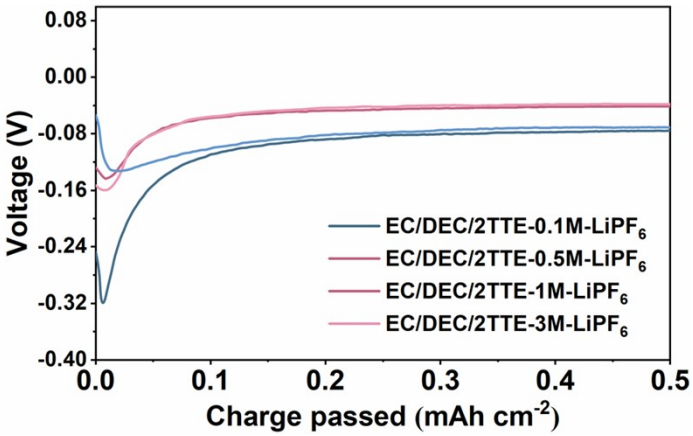

Fig. S20: Initial voltage profiles of galvanostatic lithium deposition on lithium substrate in EC/DEC-$LiPF_6$ electrolytes with different concentration.

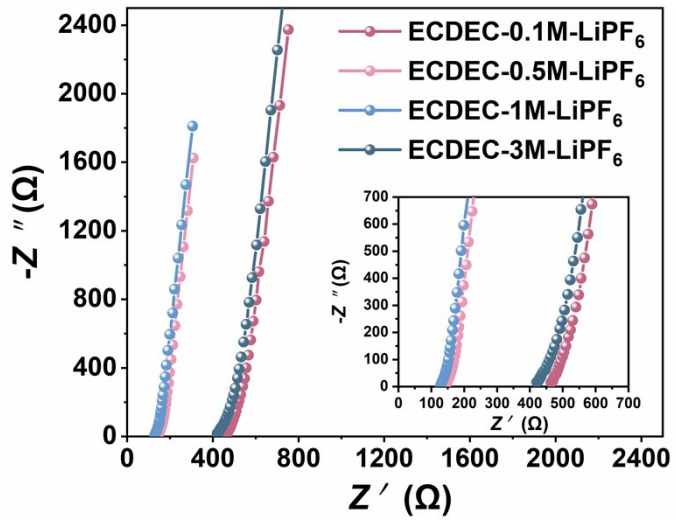

Fig. S21: (**a**) Ionic conductivity of EC/DEC-$LiPF_6$ electrolytes with different concentration.

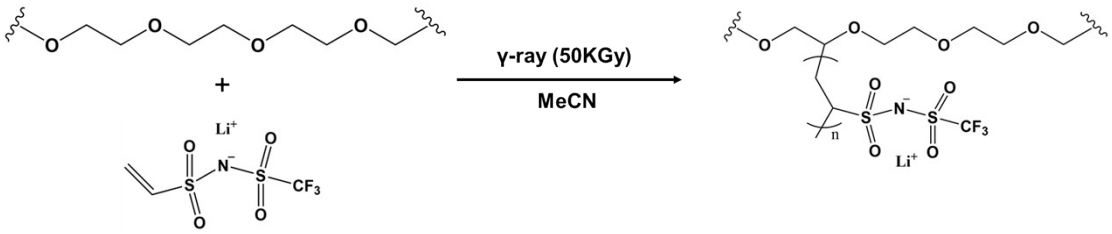

Fig. S22: Schematic illustration of the γ-ray irradiation grafting method to prepare LiTVI-PEO.

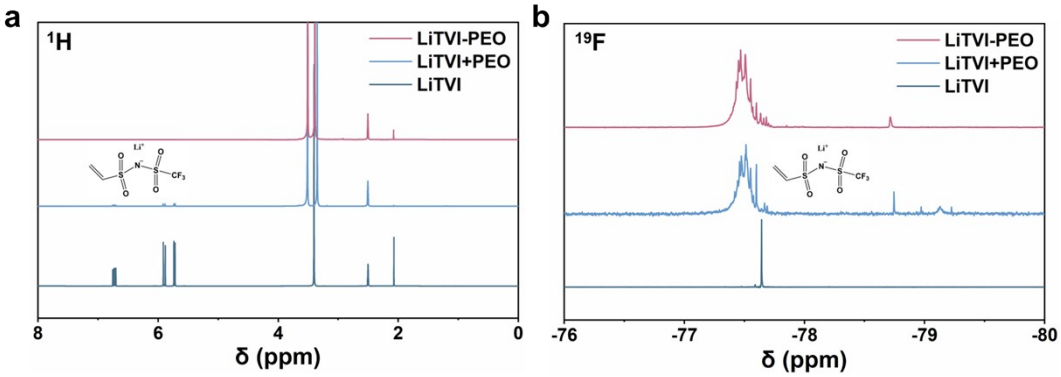

Fig. S23: NMR spectra of LiTVI-PEO: ^{1}H NMR spectra (**a**) and ^{19}F NMR spectra (**b**) of LiTVI salt, LiTVI mixed with PEO (LITV+PEO) and LiTVI-PEO. The multiple peaks centered at around 6 ppm in ^{1}H spectra can be assigned to the double bond in LiTVI and its disappearance indicating that the LiTVI is completely grafted on the PEO chains without residual monomer. The peak broadening at around -77.5 ppm in ^{19}F spectra indicating that the chemical environment of LiTVI is more complicated when grafted on PEO chains.

Fig. S24: Schematic illustration of drop-casting method to prepare HACI@Li electrode.

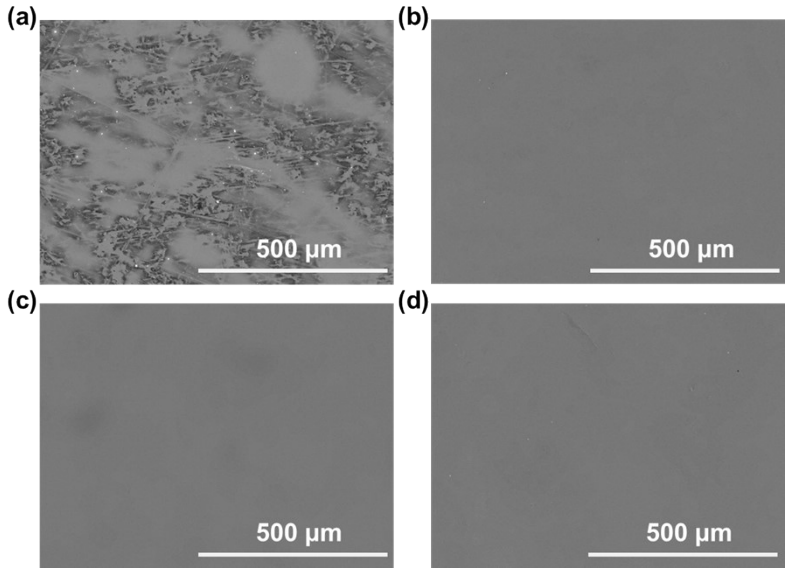

Fig. S25: Surface morphology of HACI@Li electrode with different casting amount of 20 μL(**a**), 40 μL(**b**), 60 μL(**c**) and 80 μL(**d**). The casting amount of 40 μL is enough to cover the whole Li electrode (Φ=12 mm).

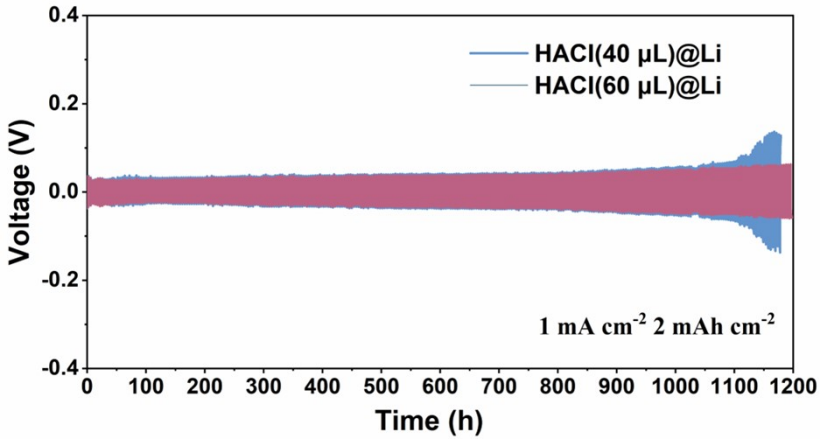

Fig S26: Cycling performance of Li||Li symmetric cells with different amount of HACI. The cycling performance of HACI@Li electrode is not further improved with the increase of the thickness of HACI.

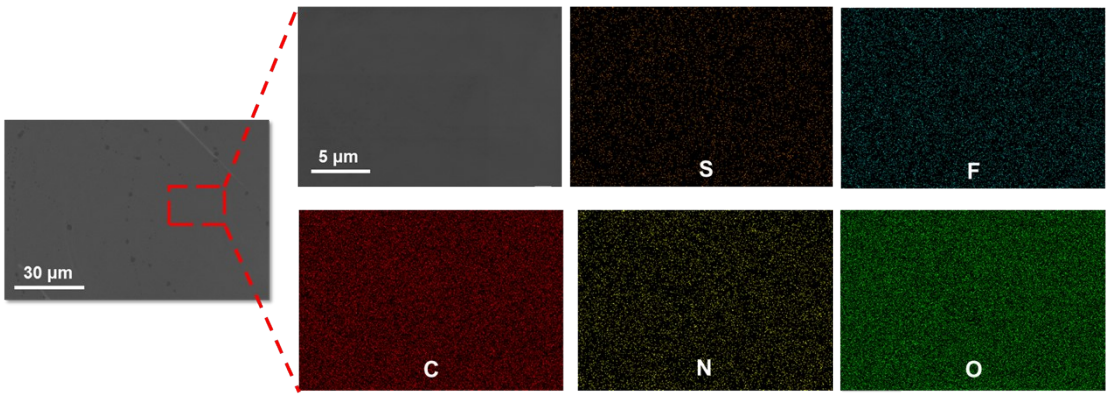

Fig. S27: Surface morphology and corresponding element mappings of HACI@Li electrode.

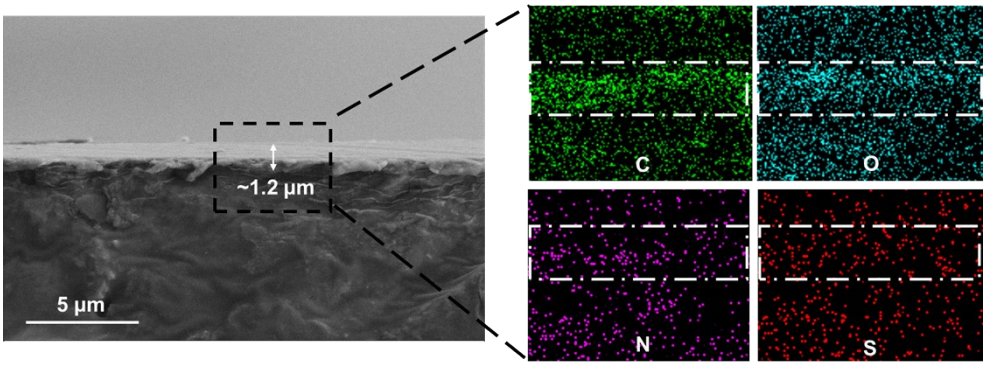

Fig.S28: Cross-sectional morphology and corresponding element mappings of HACI@Li electrode.

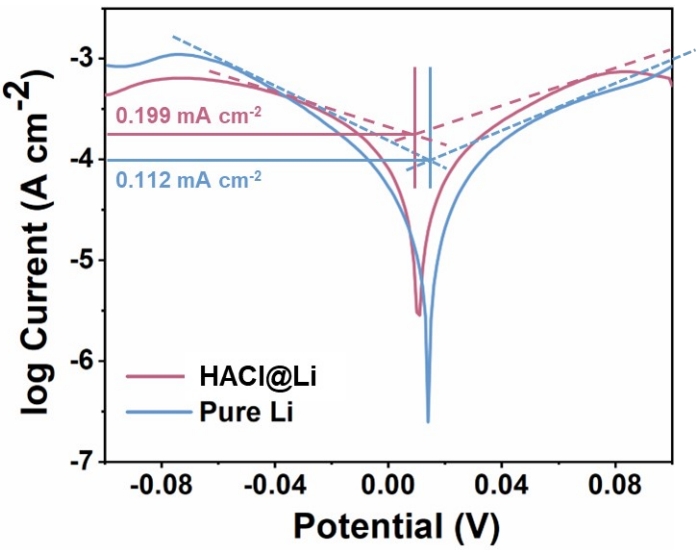

Fig. S29: Tafel curve of HACI@Li electrode and pure Li electrode.

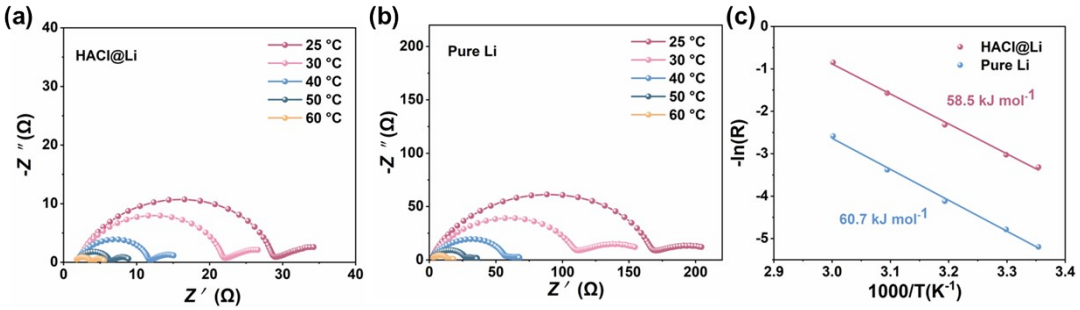

Fig. S30: EIS curves of symmetric cells at different temperatures for HACI@Li electrode (**a**) and pure Li electrode (**b**). (**c**) Corresponding Arrhenius curves and comparison of activation energies. The R_{SEI} value of different electrodes at each corresponding temperature is summarized at Table S1.

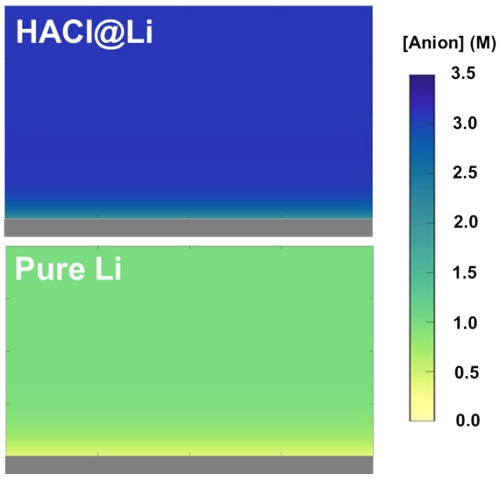

Fig. S31: FEA simulation of the anion concentration field at electrolyte/electrode interface in Pure Li electrode (upper) and HACI@Li electrode (lower).

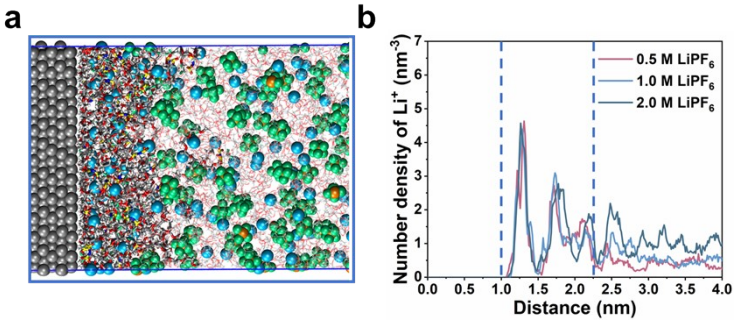

Fig. S32: MD simulation of HACI@Li electrode: **a,** simulation box of the interface of HACI@Li electrode. **b,** MD simulation of the variation of Li^+ concentration among HACI under different bulk salt concentration.

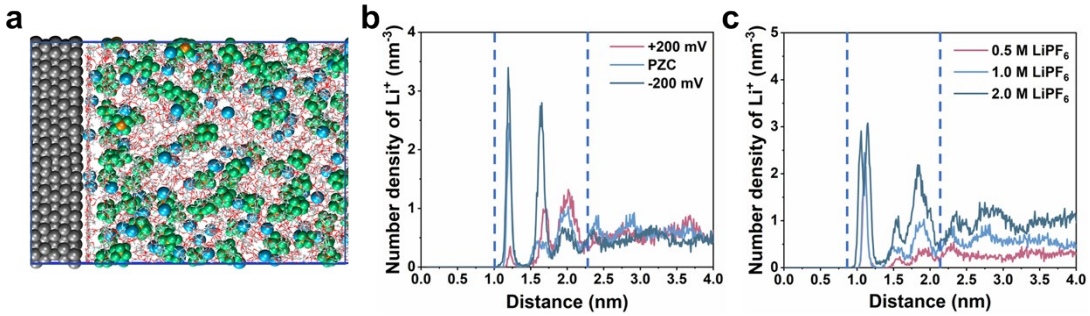

Fig. S33: MD simulation of Pure Li electrode: **a,** simulation box of the interface of Pure Li electrode. MD simulation of the variation of Li^+ concentration among interface in EC/DEC-1M-$LiPF_6$ electrolyte under different potential (**b**) and bulk salt concentration(**c**).

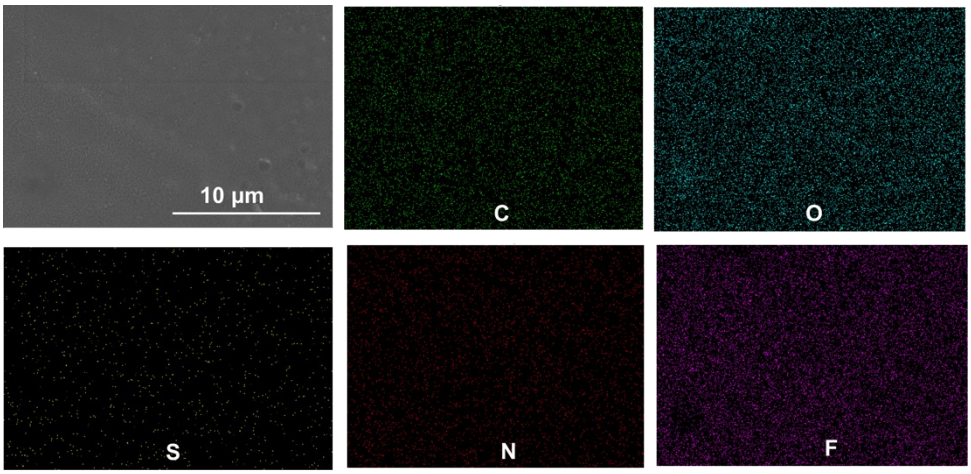

Fig. S34: Surface morphology and corresponding element mappings of HACI@Li electrode after depositing lithium of 2mAh cm^{-2}.

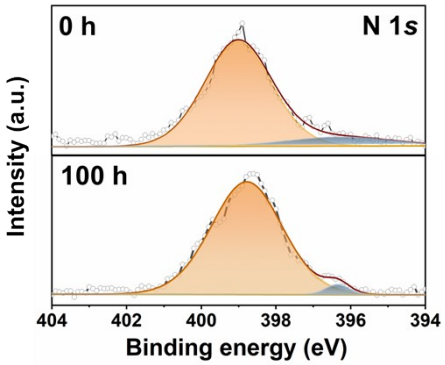

Fig. S35: N *1s* spectra of the surface of HACI@Li electrode after cycled for 100 h.

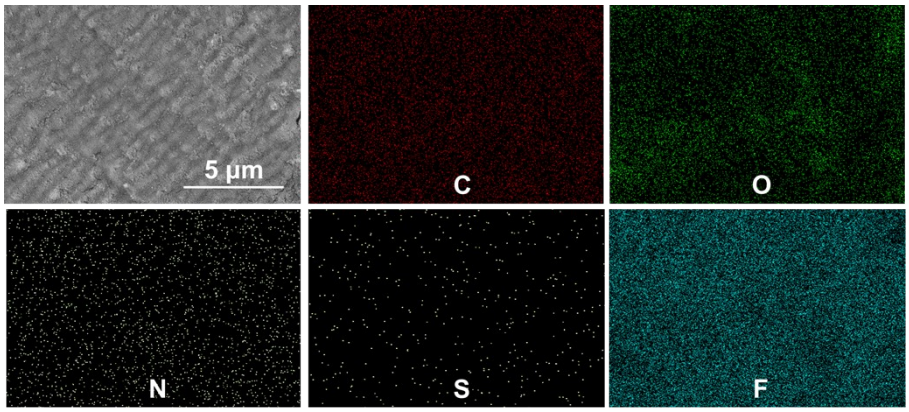

Fig. S36: Surface morphology and corresponding element mappings of HACI@Li electrode after cycled for 100 h at 1mA cm^{-2} and 2 mAh cm^{-2}.

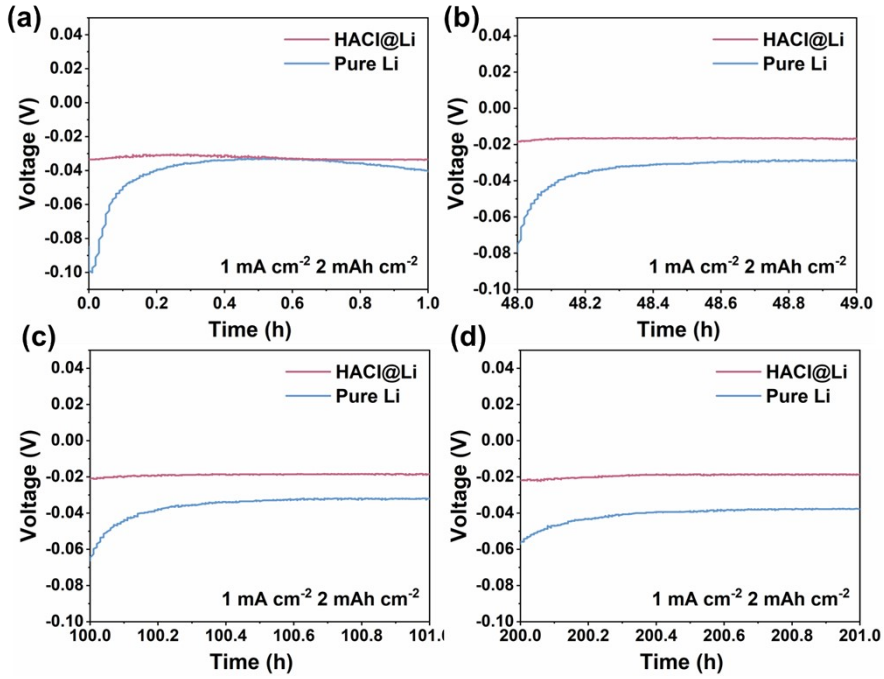

Fig. S37: Potential profiles of HACI@Li electrode and pure Li electrode after cycled for different time.

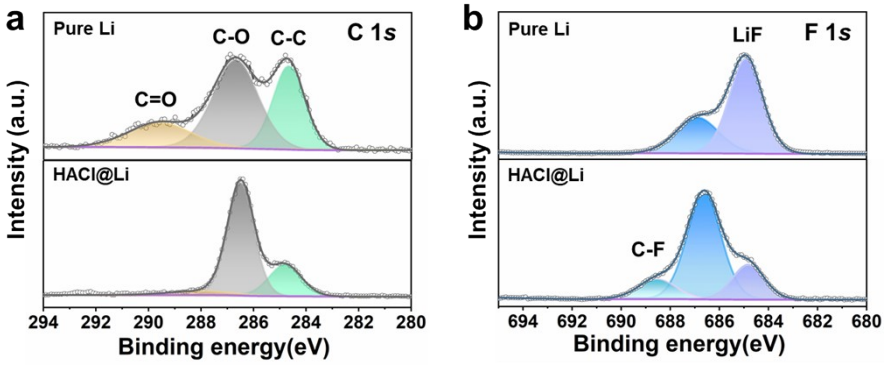

Fig. S38: XPS spectra of the HACI@Li electrode and Pure Li electrode: **a,** Comparison of C1s spectra of the surface of HACI@Li electrode and Pure Li electrode after cycled for 100 h. **b,** Comparison of F1s spectra of the surface of HACI@Li electrode and Pure Li electrode after cycled for 100 h. The peaks centered at around 284.8, 286.5, and 289.3 eV can be ascribed to C-C, C-OR, and COOR, respectively in C1s spectra.[7, 26] The peaks centered at around 684.8 and 680 eV can be ascribed to LiF and CF_3, respectively[27].

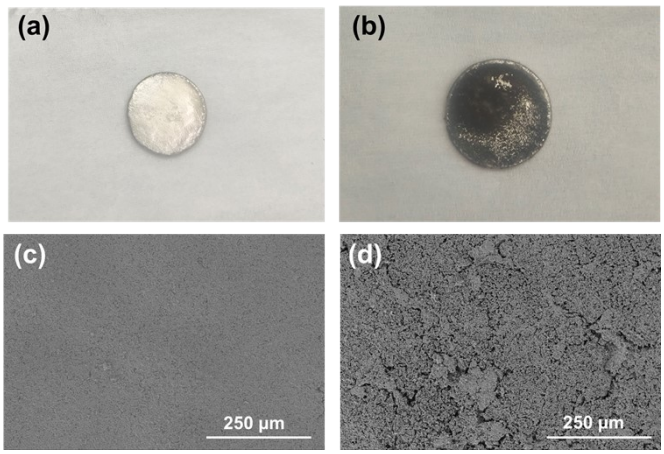

Fig. S39 Optical images and SEM images of HACI@Li electrode (**a, c**) and pure Li electrode (**b, d**) after cycled for 100 h.

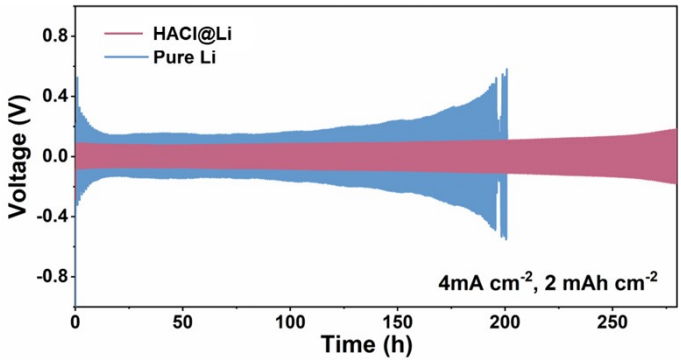

Fig. S40: Cycling performance: Cycling performance of Li||Li symmetric cells with HACI@Li electrode and pure Li electrode at current density of 4 mA cm^{-2} and capacity of 2 mAh cm^{-2}.

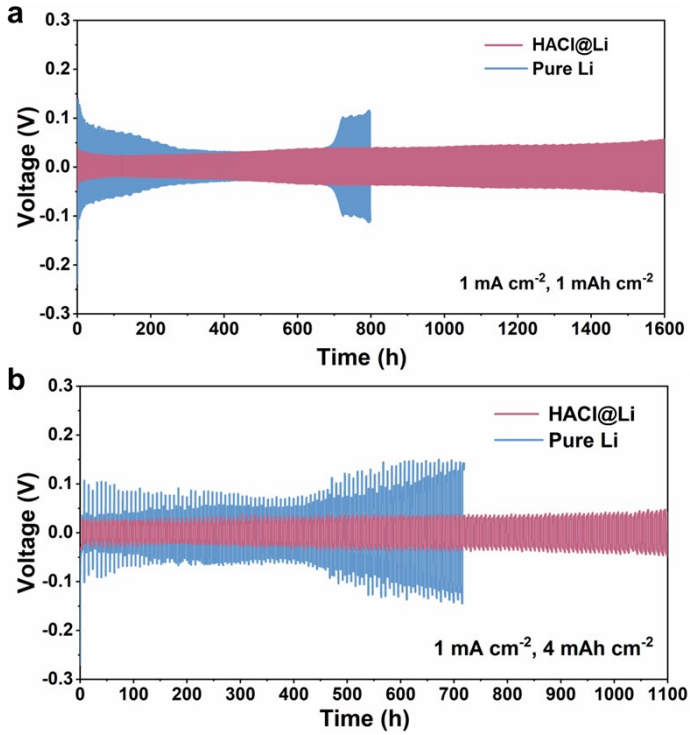

Fig. S41: Cycling performance: Cycling performance of Li||Li symmetric cells with HACI@Li electrode and pure Li electrode at current density of 1 mA cm^{-2} and capacity of 2 mAh cm^{-2} (**a**) and 4 mAh cm^{-2} (**b**).

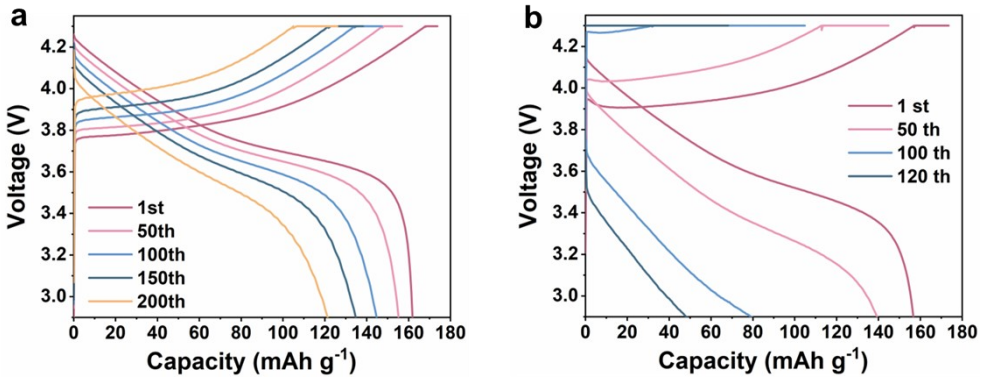

Fig. S42: Cycling performance of full cells: Capacity-voltage curve of full cells with HACI@Li anode (**a**) and pure Li anode (**b**).

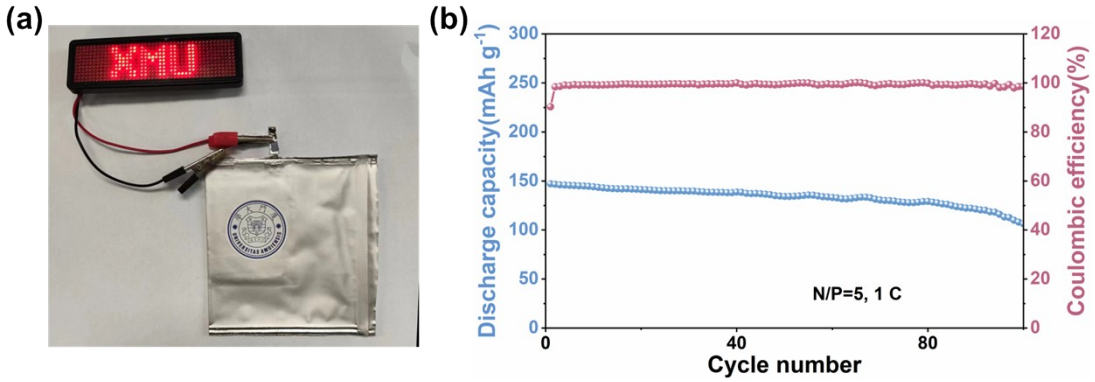

Fig. S43: Schematic illustration (a) and corresponding cycling performance of the HACI@Li|NCM523 pouch cell. The dimensions of anode and cathode are 60 × 45 mm and 56 × 43 mm, respectively.

Table S1: Electrochemical parameters of different electrolyte

	Δη(mV）	**Ionic conductivity (mS cm^{-1})**	**t_+(exp)**	**t_+(sim)**
EC/DEC-1M-$LiPF_6$	93.6	8.2	0.29	0.29
EC/DEC-1M-LiTFSI	32.0	7.0	0.38	0.36
DOL/DME-1M-LiTFSI	0	12.3	0.44	0.48

Table S2: R_{SEI} at different temperatures

T(°C)	R_{SEI}(HACI@Li)	R_{SEI}(Pure Li)
25	180.46	27.05
30	119.55	19.4
40	61.48	9.25
50	29.36	3.87
60	13.24	1.74

Table S3: Summary of symmetric cell tests of Li metal anodes protected by various reported artificial SEI layers

Artificial SEI	Electrolyte	Cycle Condition ($mA\ cm^{-2}$, $mAh \cdot cm^{-2}$)	Duration time(h)	Reference
HACI	1 M $LiPF_6$ in EC/DEC/FEC	1, 2	1200	This work
Li/P(St-MaI)	1 M $LiPF_6$ in EC/DEC/FEC	1, 1	900	3
Poly((N-2,2-dimethyl-1,3-dioxolane-4-methyl)-5-norbornene-exo-2,3-dicarboximide)	1 M $LiPF_6$ in EC/DEC/FEC	0.5, 1	300	28
Polyurea	1 M $LiPF_6$ in EC/DEC/EMC	1, 1	460	29
PR-PAA	1 M $LiPF_6$ in EC/DMC/DEC/VC	1, 1	670	30
BPPL	LiTFSI:EC=1:6	5, 1	600	31
PIL	1M LiTFSI in DME	2, 2	500	32
SP^2	1 M $LiPF_6$ in EC/DEC	1, 1	150	33
P(SF-DOL)-GO	1 M $LiPF_6$ in EC/DEC/FEC	1, 2	800	34
LiF	1 M $LiPF_6$ in EC/DEC	1, 1	600	35
PPE-Li	1 M LiTFSI in DOL/DME	2, 1	800	36
PTMEG-Li/Sn	1 M LiTFSI in DOL: DME with 1 wt % $LiNO_3$	1, 1	1000	37

Table S4: The composition and size of the simulation boxes

Composition	EC	DEC	FEC	LiTVI-PEO_{10}^-	Li	PF_6^-	Metal Zn
Zn+HACI+0.5M	672	672	148	12	180	60	3680
Zn+HACI+1.0M	672	672	148	12	240	120	3680
Zn+HACI+2.0M	672	672	148	12	360	240	3680
Zn+0.5M	672	672	148	0	60	60	3680
Zn+1.0M	672	672	148	0	120	120	3680
Zn+2.0M	672	672	148	0	240	240	3680

Table S5: Model parameters of different electrolytes.

Parameter	EC/DEC-1M-$LiPF_6$	EC/DEC-1M-LiTFSI	DOL/DME-1M-LiTFSI	EC/DEC-1M-$LiPF_6$ +10 wt% FEC
κ (mS/cm)[1]	8.2	7.0	12.3	7.8
D_+ ($\times 10^{-11}$ m^2/s)	6.57	7.48	16.4	6.25
D_- ($\times 10^{-10}$ m^2/s)	1.53	1.12	1.64	1.46
t_+^0[2]	0.29	0.38	0.48	0.3
ε_r	23	25.2	6.8	23
i_0 (A/cm^2)	0.34	1.76	4.1	1.12
α_a			0.3	
α_c			0.7[38]	

[1] κ is the ionic conductivity.

[2] t_+^0 is the transference number.

Reference

1. J. H. Baik, S. Kim, D. G. Hong and J. C. Lee, *ACS Appl. Mater. Inter.*, 2019, **11**, 29718-29724.
2. J. Evans, C. A. Vincent and P. G. Bruce, *Polymer*, 1987, **28**, 2324-2328.
3. T. Naren, G.-C. Kuang, R. Jiang, P. Qing, H. Yang, J. Lin, Y. Chen, W. Wei, X. Ji and L. Chen, *Angew. Chem. Int. Ed.*, 2023, **62**, e202305287.
4. M. J. Abraham, T. Murtola, R. Schulz, S. Páll, J. C. Smith, B. Hess and E. Lindahl, *SoftwareX*, 2015, **1-2**, 19-25.
5. W. L. Jorgensen, D. S. Maxwell and J. TiradoRives, *J. Am. Chem. Soc.*, 1996, **118**, 11225-11236.
6. T. Lu, Sobtop, Version [1.0] , http://sobereva.com/soft/Sobtop (accessed on Oct 1. 2022).
7. J. Liu, N. Pei, H. Hua, Y. Deng, H. Ma, P. Zhang and J. Zhao, *ACS Sustainable Chem. Eng.*, 2022, **10**, 9232-9241.
8. Y. Yang, H. Hua, Z. Lv, M. Zhang, C. Liu, Z. Wen, H. Xie, W. He, J. Zhao and C. C. Li, *Adv. Funct. Mater.*, 2023, **33**, 2212446.
9. C. I. Bayly, P. Cieplak, C. Wendy D and P. A. Kollman, *J. Phys. Chem.*, 1993,

97, 10269.
10. M. J. Frisch, G. W. Trucks, H. B. Schlegel, G. E. Scuseria, M. A. Robb, J. R. Cheeseman, G. Scalmani, V. Barone, B. Mennucci, G. A. Petersson, H. Nakatsuji, M. Caricato, X. Li, H. P. Hratchian, A. F. Izmaylov, J. Bloino, G. Zheng, J. L. Sonnenberg, M. Hada, M. Ehara, K. Toyota, R. Fukuda, J. Hasegawa, M. Ishida, T. Nakajima, Y. Honda, O. Kitao, H. Nakai, T. Vreven, J. A. Montgomery, Jr, J. E. Peralta, F. Ogliaro, M. Bearpark, J. J. Heyd, E. Brothers, K. N. Kudin, V. N. Staroverov, R. Kobayashi, J. Normand, K. Raghavachari, V. N. Staroverov, R. Kobayashi, J. Normand, K. Raghavachari, A. Rendell, J. C. Burant, S. S. Iyengar, J. Tomasi, M. Cossi, N. Rega, N. J. Millam, M. Klene, J. E. Knox, J. B. Cross, V. Bakken, C. Adamo, J. Jaramillo, R. Gomperts, R. E. Stratmann, O. Yazyev, A. J. Austin, R. Cammi, C. Pomelli, J. W. Ochterski, R. L. Martin, K. Morokuma, V. G. Zakrzewski, G. A. Voth, P. Salvador, J. J. Dannenberg, S. Dapprich, A. D. Daniels, Ö. Farkas, J. Foresman, J. V. B.; Ortiz, J. Cioslowski and D. J. Fox, *Gaussian 09, Revision E.01*, Gaussian, Inc., Wallingford CT, 2013.
11. T. Lu and F. Chen, *J. Comput. Chem.*, 2012, **33**, 580-592.
12. W. Humphrey, A. Dalke and K. Schulten, *J. Mol. Graphics*, 1996, **14**, 33-38, 27-38.
13. N. P. B. John Newman, *Electrochemical Systems, 4th Edition*, 2021.
14. H. Helmholtz, *Ann. Phys.*, 1879, **243**, 337-382.
15. D. L. Chapman, *Lond. Edinb. Dublin Philos. Mag. J. Sci.*, 1913, **25**, 475-481.
16. M. Gouy, *J. Phys. Theor. Appl.*, 1910, **9**, 457-468.
17. O. Stern, *Z. Elektrochem. Angew. Phys. Chem.*, 1924, **30**, 508-516.
18. M. S. Kilic, M. Z. Bazant and A. Ajdari, *Phys. Rev. E*, 2007, **75**, 021502.
19. F. Fogolari, A. Brigo and H. Molinari, *J. Mol. Recognit.*, 2002, **15**, 377-392.
20. P. D. u. E. Hückel, *Phys. Z.*, 1923, **9**, 185–206.
21. G. Zhang, H.-J. Peng, C.-Z. Zhao, X. Chen, L.-D. Zhao, P. Li, J.-Q. Huang and Q. Zhang, *Angew. Chem. Int. Ed.*, 2018, **57**, 16732-16736.
22. N. Yao, X. Chen, X. Shen, R. Zhang, Z.-H. Fu, X.-X. Ma, X.-Q. Zhang, B.-Q. Li and Q. Zhang, *Angew. Chem. Int. Ed.*, 2021, **60**, 21473-21478.
23. D. M. Seo, P. D. Boyle, R. D. Sommer, J. S. Daubert, O. Borodin and W. A. Henderson, *J. Phys. Chem. B*, 2014, **118**, 13601-13608.
24. N. Zhong, C. Lei, R. Meng, J. Li, X. He and X. Liang, *Small*, 2022, **18**, 2200046.
25. F. Qiu, S. Ren, X. Zhang, P. He and H. Zhou, *Sci. Bull.*, 2021, **66**, 897-903.
26. N.-W. Li, Y. Shi, Y.-X. Yin, X.-X. Zeng, J.-Y. Li, C.-J. Li, L.-J. Wan, R. Wen and Y.-G. Guo, *Angew. Chem. Int. Ed.*, 2018, **57**, 1505-1509.
27. S. Jiao, J. Zheng, Q. Li, X. Li, M. H. Engelhard, R. Cao, J.-G. Zhang and W. Xu, *Joule*, 2018, **2**, 110-124.
28. Y. Gao, Y. Zhao, Y. C. Li, Q. Huang, T. E. Mallouk and D. Wang, *J. Am. Chem. Soc.*, 2017, **139**, 15288-15291.
29. Y. Sun, Y. Zhao, J. Wang, J. Liang, C. Wang, Q. Sun, X. Lin, K. R. Adair, J. Luo, D. Wang, R. Li, M. Cai, T.-K. Sham and X. Sun, *Adv. Mater.*, 2019, **31**,

1806541.
30. R.-M. Gao, H. Yang, C.-Y. Wang, H. Ye, F.-F. Cao and Z.-P. Guo, *Angew. Chem. Int. Ed.*, 2021, **60**, 25508-25513.
31. C. Deng, B. Yang, Y. Liang, Y. Zhao, B. Gui, C. Hou, Y. Shang, J. Zhang, T. Song, X. Gong, N. Chen, F. Wu and R. Chen, *Angew. Chem. Int. Ed.*, 2024, **63**, e202400619.
32. Z. Huang, S. Choudhury, H. Gong, Y. Cui and Z. Bao, *J. Am. Chem. Soc*., 2020, **142**, 21393-21403.
33. Z. Huang, J.-C. Lai, S.-L. Liao, Z. Yu, Y. Chen, W. Yu, H. Gong, X. Gao, Y. Yang, J. Qin, Y. Cui and Z. Bao, *Nat. Energy*, 2023, **8**, 577-585.
34. Y. Gao, Z. Yan, J. L. Gray, X. He, D. Wang, T. Chen, Q. Huang, Y. C. Li, H. Wang, S. H. Kim, T. E. Mallouk and D. Wang, *Nat. Mater*., 2019, **18**, 384-389.
35. J. Zhao, L. Liao, F. Shi, T. Lei, G. Chen, A. Pei, J. Sun, K. Yan, G. Zhou, J. Xie, C. Liu, Y. Li, Z. Liang, Z. Bao and Y. Cui, *J. Am. Chem. Soc*., 2017, **139**, 11550-11558.
36. X. Liu, J. Liu, T. Qian, H. Chen and C. Yan, *Adv. Mater.*, 2020, **32**, 1902724.
37. Z. Jiang, L. Jin, Z. Han, W. Hu, Z. Zeng, Y. Sun and J. Xie, *Angew. Chem. Int. Ed.*, 2019, **58**, 11374-11378.
38. S. Xu, K.-H. Chen, N. P. Dasgupta, J. B. Siegel and A. G. Stefanopoulou, *J. Electrochem. Soc.*, 2019, **166**, A3456.